"Nanocasting": Using SBA-15 Silicas as Hard Templates to Obtain Ultrasmall Monodispersed γ-Fe₂O₃ Nanoparticles

E. Delahaye, V. Escax, N. El Hassan, and A. Davidson*

*University Pierre et Marie Curie, Laboratoire de Réactivité de Surface, UMR-CNRS 7609, case 178,
4 place Jussieu, 75252, Paris, France*

R. Aquino,[†] V. Dupuis, and R. Perzynski

*University Pierre et Marie Curie, Laboratoire des Liquides Ioniques et Interfaces Chargés, UMR-CNRS 7612,
case 63, 4 place Jussieu, 75252, Paris, France*

Y. L. Raikher

Institute of Continuous Media Mechanics, Ural Branch of RAS, 1 Korolyov Street, Perm, 614013 Russia

This work describes the use of mesoporous SBA-15 silicas as hard templates for the size-controlled synthesis of oxide nanoparticles, with the pores acting as nanoscale reactors. This fundamental work is mainly aimed at understanding unresolved issues concerning the occurrence and size dependence of phase transitions in oxide nanocrystals. Aqueous solutions of $Fe(NO_3)_3 \cdot 9H_2O$ are deposited inside the pores of SBA-15 silicas with mesopore diameters of 4.3, 6.6, and 9.5 nm. By calcination, the nitrate salt transforms into FeO_x oxides. The XRD peaks of nanocrystals are broad and overlapping, resulting in ambiguities attributed to a given allotropic variety of Fe_2O_3 (α, ε, or γ) or Fe_3O_4. The association of XRD, SAED, and Raman information is necessary to solve these ambiguities. The metastable γ-Fe_2O_3 variety is selectively formed at low Fe/Si atomic ratio (ca. 0.20) and when a low calcination temperature is used (773 or 873 K followed by quenching to room temperature once the targeted temperature is reached). The small size dispersion of the patterned nanoparticles, suggested on a local scale by TEM, is confirmed statistically by magnetic measurements. The nanoparticles have a superparamagnetic behavior around room temperature. Their magnetic moments (from 220 to 370 mB), their sizes (from 4.0 to 4.8 nm), and their blocking temperatures (from 36 to 58 K) increase with the silica template mesopore diameter. Their magnetic properties are compared to those of standard γ-Fe_2O_3 nanoparticles of similar size, obtained by coprecipitation in water and stabilized by a citrate coating.

1. Introduction

Decreasing the size of γ-Fe_2O_3 particles down to the nanometric range results in magnetic and chemical properties (thermal stability, reactivity, catalytic applications) which are not achieved with the bulk oxide. Fundamental work is still necessary to understand and control these properties, since when entering the nanometric dimension, there is a complex interplay between finite size effects, interface effects, and interparticle interactions.[1−3] For individualized particles, the reduction of lattice symmetry at the surface yields to an enhancement of the magnetic surface anisotropy,[4−6] which, despite recent measurements[7] and simulations,[8] is not yet completely understood.

γ-Fe_2O_3 nanoparticles can be prepared by laser pyrolysis,[9] by the vaporization−condensation process,[10] and by coprecipitation in solution, starting from Fe(II) and Fe(III) salt precursors,[7,11] for instance. The sol−gel technique can also be used to obtain iron oxide FeO_x nanoparticles embedded in amorphous silica.[12−16] In that case, an iron precursor and a silicon alkoxide (tetraethoxyorthosilane, TEOS, for instance) are mixed. A gelation time is necessary for the hydrolysis/condensation of

the silica precursor at controlled pH, which leads to the amorphous silica network. After this gelation time, iron oxide particles are generated by thermal treatment and remain trapped inside disordered pores. Under selected experimental conditions, this mode of preparation gives Fe_3O_4, γ-Fe_2O_3,[12−16] or ε-Fe_2O_3[12−16] nanoparticles dispersed inside silica. Traces of α-Fe_2O_3[15] have also been observed. This sol−gel preparation has several limitations: (i) the FeO_x nanoparticles are not always fully accessible, hampering fundamental work about adsorption processes or applied catalytic applications, (ii) the pores of the aperiodic silica template are not well-calibrated (ranging typically between 2 and 140 nm in diameter in ref 12) yielding to a broad distribution in size of FeO_x nanocrystals, and (iii) the final materials lack long-range order. As an alternative to sol−gel techniques, several groups have tried to pattern iron oxide particles in periodic mesoporous silicas: two-dimensional hexagonal (SBA-15[17,18] and MCM-41[19−22]) and cubic (MCM-48[23]) silicas. The pores of these silicas are well-calibrated, with mesopore diameters which can be adjusted between 4 and 10 nm and with a pore size distribution not exceeding ±1 nm. Using these ordered silicas to grow inorganic objects of controlled dimensions is known as the "nanocasting" strategy and has been pioneered by the Ryoo group for the preparation of ordered carbon.[24] For the patterning of iron oxides, several

---

* To whom correspondence should be addressed. E-mail: davidson@ccr.jussieu.fr.
† Permanent address: Complex Fluid Group, Instituto de Fisica, Universidade de Brasilia, Caixa Postal 04455, 70919−970, Brasilia DF, Brazil.

iron precursors, deposition techniques, and calcination conditions, all leading to hematite, have been reported.

The goal of the present work is to define experimental conditions under which another allotropic variety, maghemite, is formed by "nanocasting" inside the calibrated pores of SBA-15 silicas. To avoid the growth of large FeO_x iron oxide particles outside the silica grains, the iron precursor (iron nitrate) is deposited inside the mesopores of SBA-15 silicas using the two-solvents technique already described elsewhere and successfully applied to other oxides (manganese oxides, for instance[25]). Two series of samples are described. For the first series, the structural parameters of the silica template are varied (mesopore diameters from 4.3 and 9.5 nm) for a given Fe/Si atomic ratio (near 0.20). For the second series, the Fe/Si atomic ratio is increased from 0.22 up to 0.67 for a given silica template (mesopore diameter ca. 6.6 nm). The silica and Fe-loaded SBA samples are characterized using a multiscale then multitechnique approach, combining textural, N_2 sorption, structural, X-ray diffraction, and transmission electron microscopy (TEM) images, coupled with high-resolution TEM (HR-TEM) and selected area electron diffraction (SAED). For its ability to differentiate among Fe_3O_4, α-Fe_2O_3, and γ-Fe_2O_3, spectroscopic information given by micro-Raman is also described. Finally, the magnetic properties of the samples containing maghemite nanoparticles are compared to those of γ-Fe_2O_3 nanoparticles, of similar size, obtained by coprecipitation in water and stabilized by a citrate coating.[11] Special emphasis is given to the comparison of crystallinity and of interface (or surface) effects in the two series of FeO_x nanoparticles.

2. Experimental Section

2.1. Materials. *Preparation and Main Characteristics of the SBA-15 Silica Templates.* SBA-15 silicas are synthesized in the conditions reported by G. D. Stucky and his team in 1998.[26] P123, a triblock copolymer, is used as structuring agent. The first silica, labeled SBA-A, is obtained without any hydrothermal treatment. The second and third ones, labeled SBA-B and SBA-C, are obtained after a standard hydrothermal treatment for 1 day, respectively, at 373 and 403 K. SBA-A, SBA-B, and SBA-C samples are further calcined in a muffle oven at 773 K for 5 h (heating rate of 2 K/min, static conditions, in air) to eliminate the structuring agent and liberate their pores.

Introduction of the Iron Nitrate Precursor within the Pores. The "two solvents" method, detailed in ref 25, derives from incipient wetness impregnation techniques and is based on the suspension of dried silica inside a first hydrophobic solvent (hexane) before the addition of a volume of aqueous solution containing the iron precursor and set equal to the porous volume of the silica used as a hard template (the one determined by N_2 sorption). An aqueous $Fe(NO_3)_3 \cdot 9H_2O$ solution of concentration of 1 mol.L^{-1} is used to obtain Fe-loaded SBA-A, SBA-B, and SBA-C samples. With SBA-B, three solutions of increasing concentrations in iron nitrate (from 1 to 3 mol.L^{-1}) are used. In the obtained samples, atomic Fe/Si ratios range between 0.22 and 0.67. After drying in air for 12 h, the iron nitrate decomposition is induced by calcination in air. After this treatment, the salt is fully decomposed, as indicated by the absence of a characteristic nitrate infrared band at 1380 cm^{-1}. Most of the samples are calcined at 773 or 873 K (2 K/min), then quenched to room temperature. To help the identification of FeO_x oxides in XRD, two selected samples are calcined in more stringent conditions. The first one is calcined at 873 K, with a heating rate of 2 K/min, the final temperature being kept for 6 h (SBA-B, atomic Fe/Si ratio of 0.45) before quenching

TABLE 1: Main Characteristics of the Silica Templates (as obtained by N_2 sorption)

silica template	specific surface area (BET, $m^2 \cdot g^{-1}$)	porous volume ($cm^3 \cdot g^{-1}$)	mesopore diameter (BJH, desorption, nm)
SBA-A	622	0.67	4.3
SBA-B	936	1.24	6.6
SBA-C	730	1.54	9.5

to room temperature. The second one is calcined at 1373 K, with a heating rate of 2 K/min, the final temperature being maintained 3 h before cooling down to room temperature at 2 K/min (SBA-B, atomic Fe/Si ratio ~0.53). Note that, in the two last samples, the silica template has lost its periodicity, and its mesopores have collapsed (N_2 sorption specific surface area, 18 m^2/g; selected TEM images are shown in Supporting Information 1).

All the Fe-loaded samples are further labeled Fe-SBA-*X-x-y* with *X* standing for A, B, or C; *x* standing for 773 or 873 (773 or 873 K then quenching), 773,6 (773 K maintained for 6 h), and 1373,3 (1373 K maintained for 3 h); and *y* for the atomic Fe/Si ratio obtained by chemical analysis (Centre de microanalyse du CNRS, Solaize, France).

Preparation of Ferrofluid Standards. The ferrofluids (FF), used here as reference standards, are dispersions of maghemite (γ-Fe_2O_3) nanoparticles in water. Magnetite nanoparticles are chemically synthesized by coprecipitation of $FeCl_2$ and $FeCl_3$ in alkaline medium.[11] These nanoparticles are further oxidized by ferric nitrate in nitric acid and yield to cationic maghemite nanoparticles dispersible in nitric acid at pH 1.2. They are then coated with citrate molecules, which ensure a negative charge at neutral pH. At the end of the chemical synthesis, the diameters of the particles are not well-calibrated. The polydispersity is reduced using a routine size-sorting procedure.[27] This fractionation process is based on a colloidal phase separation, dependent on the size of the nanoparticles, and induced by an increase of ionic strength. Three samples FFA, FFB, and FFC, with nanoparticles of different mean diameter, are then obtained.

2.2. Experimental Methods. N_2 sorption isotherms at 77 K are measured with an ASAP 2010 apparatus (Micromeritics, Norcross). Prior to the experiment, the samples are dehydrated at 323 K for a few hours and then at 423 K for more than 6 h under a vacuum better than 10^{-4} Torr. The single point total pore volume V_p is estimated for a relative pressure, P/P_0 (P_0 saturation vapor pressure of N_2), close to unity. The specific surface area, S_{BET}, is obtained by using Brunauer–Emmett–Teller equations in the relative pressure range (0.05–0.25). The average diameter of primary mesopores, labeled D_{BJH}, in Tables 1 and 2, is derived from the maximum of the pore size distribution curve obtained by applying the Barret, Joyner, and Halenda formula to the desorption branch of the isotherm. This technique is known to underestimate mesopore diameters, but relative variations among samples should be correct.[28]

Only X-ray diffraction at wide angles, WAXS, measured on a laboratory powder diffractometer are described here (Siemens D500 diffractometer, Cu Kα anticathode). We have also checked at small angles that the 2D hexagonal structure of our silica templates was maintained at all the steps of synthesis (M. Impéror-Clerc, Laboratoire de Physique des Solides, Orsay, France, unpublished results).

Two transmission electron microscopes are used, a JEOL JEM-100 CX II UHR operating at 100 keV to observe the morphology of the samples and a JEOL JEM-2010 UHR operating at 200 keV for high-resolution TEM (HR-TEM) and energy dispersive X-ray spectroscopy (EDXS) measurements.

Nanocasting

J. Phys. Chem. B, Vol. 110, No. 51, 2006 **26003**

TABLE 2: Main Characteristics of Selected Fe-Loaded SBA Samples (as obtained by N$_2$ sorption)

sample	specific surface area[a] (m$^2 \cdot$g^{-1})	$\Delta S/S°$ accessible surface[b] (%)	porous volume[c] (cm$^3 \cdot$g^{-1})	$\Delta V/V°$ accessible porous volume[d] (%)	mesopore diameter BJH, desorption[e] (nm)
Fe−SBA-A-773−22	490	78	0.47	56	4.5 + 4.0[f]
Fe−SBA-B-773−27	732	78	1.19	96	5.8
Fe−SBA-C-773-21	697	95	1.39	90	7.8 + 4.0[f]
Fe−SBA-B-773−67	791	85	1.15	93	6.0 + 4.0[f]

[a] Obtained using the Barrett Emmet Teyler, BET, formulation. [b] Difference between the specific surface area measured before and after Fe loading, divided by the specific surface area of the blank silica. [c] Measured on the isotherm, for a relative pressure in nitrogen, $P/P°$ ca. 0.98. [d] Difference between the porous volume measured before and after iron loading divided by the porous volume of the blank silica. [e] Main mesopore diameter obtained by applying the Brunauer Joyner and Halenda BJH model to the desorption branch of the isotherm. [f] This peak is an artifact and reflects the tensile strength effect of the adsorbate (Gregg, S. J.; Sing, K. S. W. In *Adsorption, Surface Area and Porosity*, 2nd ed.; Academic Press: New York, 1982; p 154). It suggests a distribution of pores smaller than 4 nm rather than pores having this well-defined dimension.
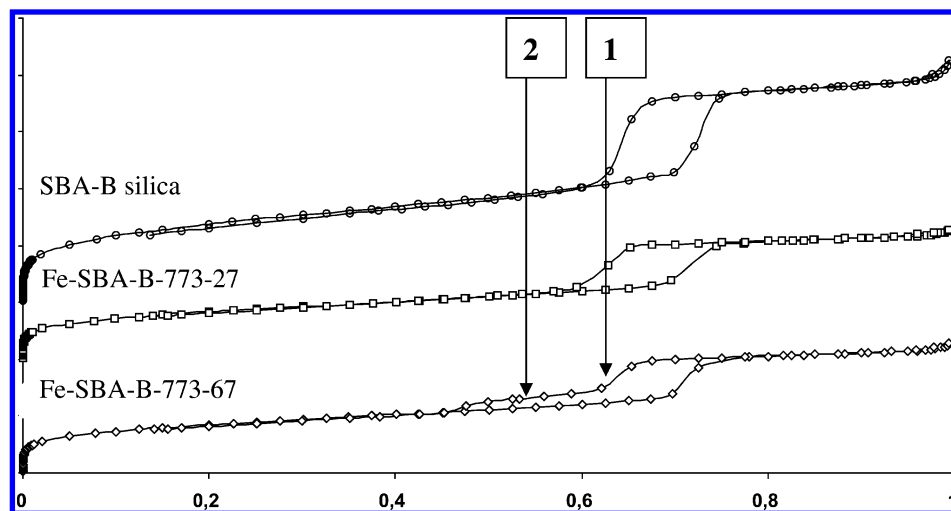

Figure 1. N$_2$ sorption isotherms of ○ blank SBA-B silica and selected Fe-loaded samples: □ Fe−SBA-B-773−27; ◇ Fe−SBA-B-773−67 (*y*-axis, adsorbed volume of N$_2$ at standard temperature and pressure, vertical increment of 200 cm^3/g added to normalized curves).

For TEM observations, samples are prepared either by dispersing the powders in dry ethanol, deposited on a copper grid covered with a carbon thin film, or by including within a resin for the preparation of ultrathin sections of the silica grains. In the latter case, a few milligrams of powder are deposited in the bottom of a Beem capsule. Some embedding resin (Epon 812, Roth) is added and polymerized for 48 h at 333 K. The polymerized blocks are cut using a diamond knife. Ultrathin sections about 70 nm thick are deposited on copper grids. On these sections, the main axes of the silica grains are randomly oriented. On the images which are presented here, only silica grains cut either parallel to their main axis (longitudinal) or perpendicular to this axis (transversal) are selected. HR-TEM images are recorded with magnifications from 470 000 up to 800 000. Selected area electron diffraction (SAED) images were collected using an analysis spot of 250 nm in diameter. For micro-Raman spectroscopy, we use a Kaiser Optical System equipped with a laser diode working at 785 nm. Unwanted heating effects induce FeO$_x$ phase transformations.[12,29] To avoid these effects, the power on the sample is systematically set lower than 30 mW (10 mW at the sample), and we have carefully checked that the signals are not affected under these conditions (compare the spectra of ϵ-Fe$_2$O$_3$ collected at 30 and 10 mW given in Supporting Information 2). Reference spectra of hematite (commercial analytical grade) and of a conventional ferrofluid (maghemite as determined by XRD, prepared in the LI$_2$C laboratory), collected in the same conditions, are also presented.

Various magnetization measurements are performed with a SQUID magnetometer (superconducting quantum interference device, Quantum design, MPMS). Zero field cooled (ZFC) and field cooled (FC) magnetic magnetizations are measured between 5 and 300 K under various magnetic fields. Hysteresis loops are recorded at 5 and 30 K between ±4 × 10^3 kA/m (field cooled under 16 kA/m (or ZFC) for Fe-loaded SBA-15 samples and ZFC for the ferrofluids). Finally, room-temperature magnetization are recorded for SBA-15 samples and ferrofluid standards. Inside the ferrofluid solutions, because of the rotational degree of freedom of the dispersed nanoparticles, these measurements allow us to determine the dipolar interaction parameter of the dispersions and the distribution of magnetic diameter of the magnetic nanoparticles (assimilated here to a log-normal distribution).[30] The mean particle diameter $d_0 =$ exp-($\langle \ln d \rangle$) and its standard deviation σ are collected in Table 5. The volume fraction Φ of the magnetic nanoparticles in the ferrofluid samples is determined using the iron chemical titration (see Table 5). This volume fraction is systematically kept low enough for dipolar interparticle interaction to be negligible in the range of temperatures 5 K $\leq T \leq$ 300 K. For SBA-15 samples, the volume fraction Φ of magnetic material is deduced from the quantity of iron introduced at the synthesis, assuming a density on the order of 5 × 10^3 kg/m^3 for the obtained oxide.

3. Results

3.1. Characterization of the Blank SBA-15 Silicas. Some characteristics of SBA-A, SBA-B, and SBA-C silicas are gathered in Table 1. N$_2$ sorption isotherms of type IV are recorded with the three silicas. The three isotherms present a type A hysteresis loop in their high-pressure part (Figure 1, ref 26). The mesopore diameter increases with the temperature of hydrothermal treatment. Important variations of the overall porous volume, V_p, and the specific surface area, S, are also

observed. The decrease of specific surface area between SBA-B and SBA-C, unexpected on a pure geometrical model (if only variations of mesopore diameters and a pure geometrical model are considered) suggests that the SBA-C sample contains a minor fraction of amorphous (and then nonporous) silica.

3.2. Characterization of the Fe-SBA-*X-x-y* Samples. *Location of FeO$_x$ Particles (inside/outside SBA-15 silica grains).* Main characteristics of selected Fe-SBA-*X-x-y* samples are gathered in Table 2. To avoid the unwanted "dilution" due to the presence of nonporous iron oxides within the powders, the specific surface area and porous volumes are expressed by grams of silica and corrected from the weight fraction due to Fe$_2$O$_3$ particles, taking molecular weight of 60.08 for silica and 159.69 g·mol^{-1} for iron oxide.

N$_2$ sorption isotherms recorded on SBA-B in its siliceous form and after Fe loading are compared in Figure 1. On Fe-SBA-B-773-27 and Fe-SBA-C-773-21 samples (prepared with diluted impregnation solution 1 mol·L^{-1}), the shape of the isotherm is not significantly modified after the Fe loading. The accessible porous volume and specific surface area decrease, but this is not enough to prove that iron oxide particles have grown inside the pores, making them inaccessible to nitrogen molecules. Indeed, large oxide particles generated on the outlet of silica grains can also plug the mesopore entrance. However, three independent observations confirm that some of the iron oxide particles are located inside the pores: (1) For a given iron amount, the specific surface area decrease follows the structural parameters of the silica hard template. This decrease is more marked with SBA-B (78% of the porous volume remaining accessible, smaller initial V_p) than SBA-C (95%, larger initial V_p). (2) The diameter of the mesopores obtained by applying the BJH formulas to the desorption branch of the isotherm decreases after iron introduction. (3) The hysteresis loop becomes broader. The desorption branch of the isotherm shifts to lower pressure, whereas the adsorption branch is not significantly changing. As suggested by Ravikovitch and co-workers,[31] this behavior indicates the coexistence of open and partially closed mesopores. On two other samples, the Fe-SBA-A-773-22, with a smaller porous volume but at a similar Fe loading, and the Fe-SBA-B-773-67, with the same porous volume but at a higher iron loading, the shape of the isotherm becomes significantly different. A peculiar two-step behavior is observed on the hysteresis loop. On one hand, the remaining empty mesopores behave as usual and give a hysteresis loop that ends near $P/P^0 = 0.6$ (arrow 1). On the other hand, partially blocked mesopores are associated with a hysteresis loop which close before, near $P/P^0 = 0.4$ (arrow 2). As indicated in the literature for zirconia containing SBA-15 silicas,[32] these two steps indicate that large oxide particles have grown in the pores of the silica host, yielding to a typical ink-bottle adsorption/desorption behavior. Several particles are located in the same mesopore, and the volume trapped between them can only be probed through small necks. This observation is critical, since it suggests that the patterned FeO$_x$ particles are smaller than the mesopore dimensions of the silica host.

Selected TEM images of the Fe-SBA-A-773-22, Fe-SBA-B-773-27, Fe-SBA-C-773-21, Fe-SBA-C-873-21, and Fe-SBA-B-773-67 samples are presented in Figures 3 and 4. Due to electronic density contrasts, iron oxides particles appear in black and silica walls in gray. The two-dimensional hexagonal structure of the silica template is preserved after the Fe loading and the crystallization of iron oxide particles. As evidenced on an ultrathin section of Figure 3B, nanoscale iron oxide particles are trapped within the pores. Note that (i) if some of the pores
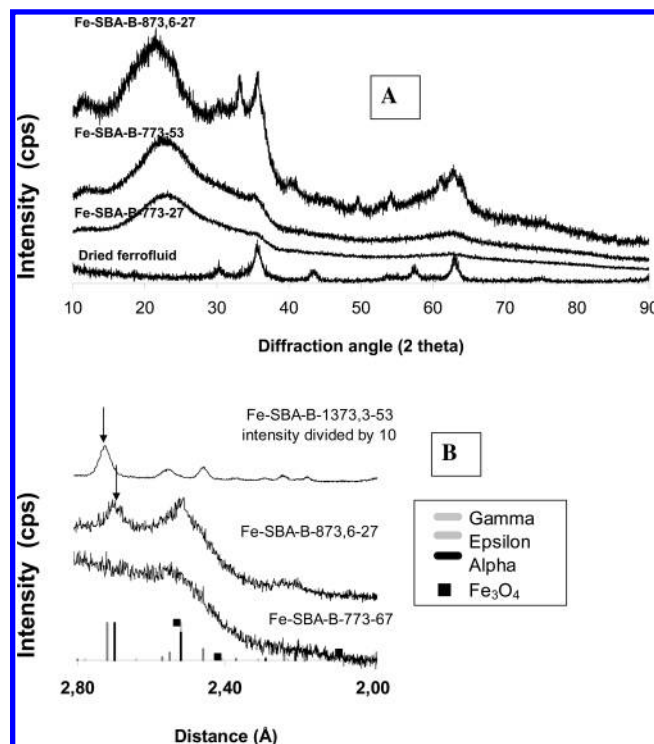

Figure 2. X-ray diffractograms of selected Fe-loaded SBA-B silicas. Part A: *x*-axis, 2θ, diffraction angle; *y*-axis, normalized intensity (cps) adding vertical increments. Part B: *x*-axis, in distances; *y*-axis, peaks relative intensity with a reference value of 100 given to the most intense diffraction. Stick diagrams of the JCPDS files of α-Fe$_2$O$_3$ (01-071-5088), γ-Fe$_2$O$_3$ (00-039-1346), ϵ-Fe$_2$O$_3$ (16-653), and Fe$_3$O$_4$ (01-079-0416) are indicated. For comparison, the X-ray diffractogram measured on a dried ferrofluid (maghemite) is also given in part A.
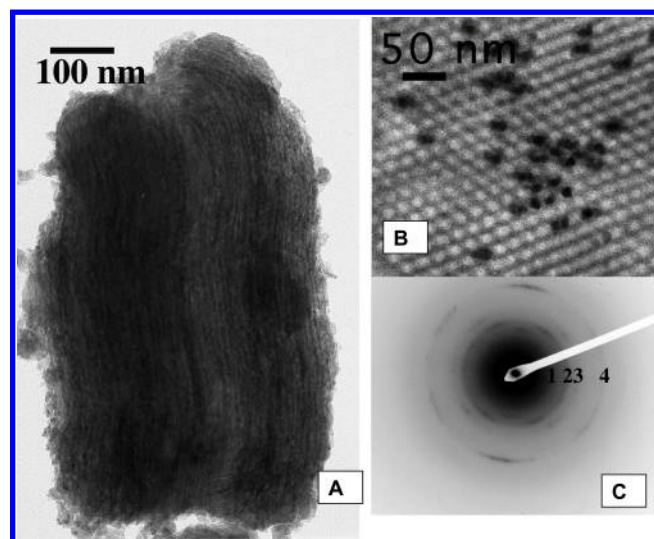

Figure 3. Fe-SBA-C-873-21 sample. Part A: typical TEM image of a silica grain with its main axis perpendicular to the electron beam; iron oxide nanoparticles in dark; silica walls in gray. Part B: ultrathin section to prove that the iron oxide particles are located inside the pores and not on the external surface of the silica grain; silica grain with its main axis parallel to the electron beam; empty and filled mesopores with a preserved two-dimensional structure. Part C: SAED at the bottom of the grain shown in the part A; distances calibrated on the basis of independent measurements on gold; attribution to maghemite: ring 1, 311; ring 2, 400; ring 3, 422; ring 4, 511.

are filled, others are empty. This was expected since the density of maghemite is 4.845 (JCPDS 00-039-1346). With this value, 61 mmol of Fe are necessary to obtain the volume of iron oxide necessary to fill a porous volume ca. 1 cm^3, whereas only 3 to

Nanocasting

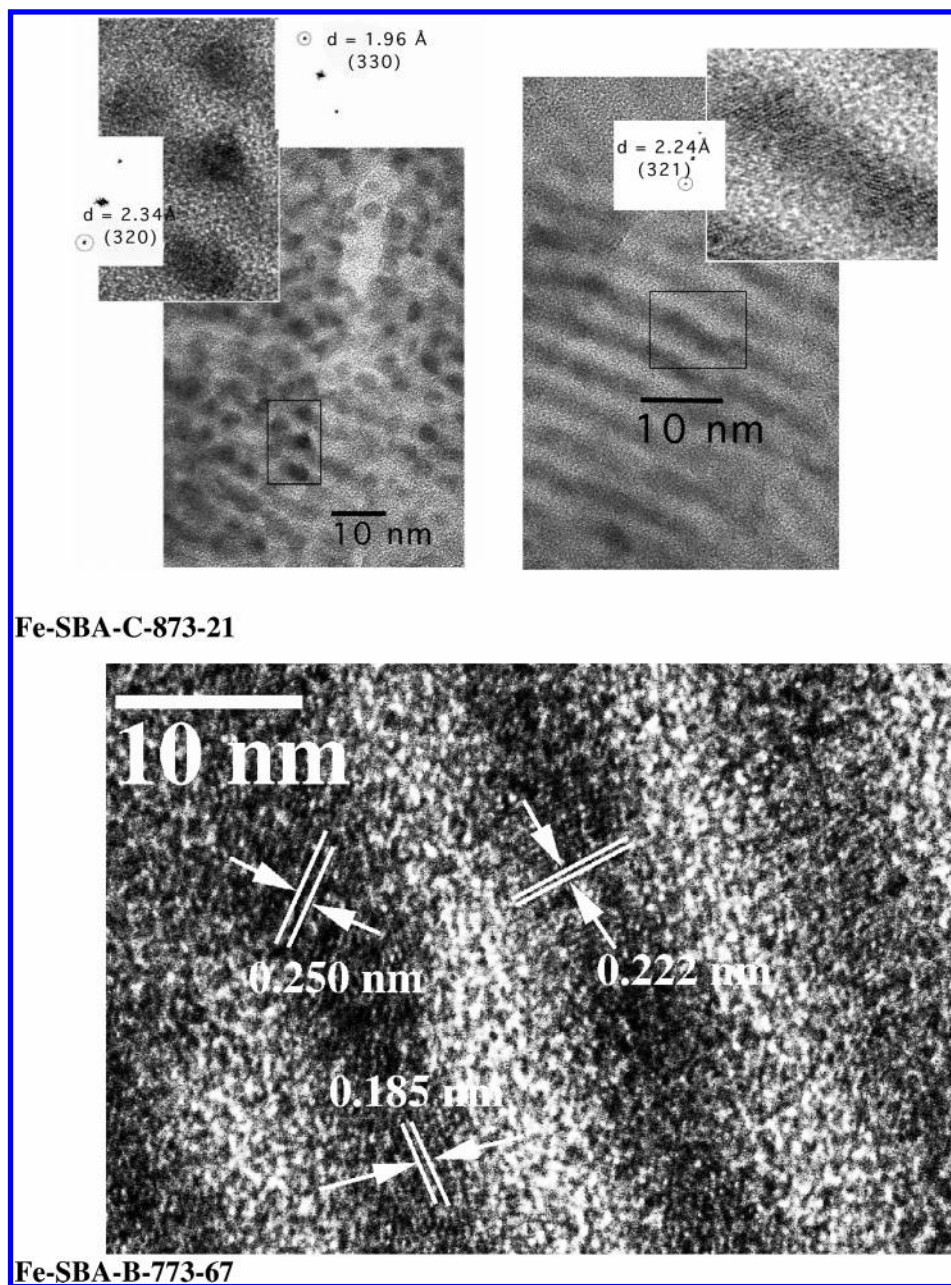*J. Phys. Chem. B, Vol. 110, No. 51, 2006* **26005**

Figure 4. Selected HR-TEM images of the Fe-SBA-B-773-67 and Fe-SBA-C-873-23 samples.

12 mmol have been introduced here. (ii) No large oxide particles outside the silica grains can be distinguished. (iii) Some of the FeO_x particles are not fully plugging the pores. TEM results agree then with N_2 sorption results and show that guest FeO_x nanoparticles have grown inside SBA-15 silica grains and that some of these particles are smaller than the mesopores of the silica host.

Crystallographic Nature of the Patterned FeO_x Iron Oxide Particles. Depending upon preparation conditions (atmosphere, heating rate, final temperature), the thermal decomposition of iron nitrate in silicas containing FeO_x nanoparticles gives either Fe_3O_4, magnetite, or one of the allotropic varieties of Fe_2O_3: maghemite, the spinel γ-type, hematite, the corundum α-type or the ϵ-type.[12−16] Due to the easy reoxidation of Fe(II) centers, magnetite is not stable in air. Because of the particles trapping inside silica, we have however decided to keep this oxide in consideration. The structures of Fe_3O_4 and γ-Fe_2O_3 are closely related. Their spinel unit cells contain two kinds of cationic sites: type A surrounded by four oxygen anions and type B surrounded by six oxygen anions. In a direct spinel structure, divalent cations are located in tetrahedral A sites. As recently summarized in ref 12, Fe_3O_4 which contains Fe(II) and Fe(III) cations has an inverse spinel structure with Fe(II) cations located in octahedral sites. The structure of γ-Fe_2O_3 is related, with cationic vacancies being located in octahedral sites or distributed randomly between octahedral and tetrahedral sites. The transformation of Fe_3O_4 into a vacancy containing γ-Fe_2O_3 is possible at rather low temperatures.[33] The γ-Fe_2O_3 polymorph transforms to α-Fe_2O_3 by calcination if agglomeration takes place or to ϵ-Fe_2O_3 if agglomeration is avoided.[16] The last polymorph, ϵ-Fe_2O_3, has been observed for iron oxide nanoparticles dispersed in silica, and its formation seems to require heat treatments at high temperatures, 1373 K in refs 15 and 16, for instance.

The diffractogram of the Fe-SBA-B-1373,3-53 sample treated at 1373 K is easy to analyze. Only narrow and well-defined diffractions (Supporting Information 3) which can be assigned to well-crystallized nanoparticles of the ϵ-Fe_2O_3 variety are

TABLE 3: Ambiguities of Attributions between Fe_3O_4 and the α, γ, and ε Allotropic Varieties of Fe_2O_3 Based on X-ray and Electron (SAED) Diffractions[a]

		Magnetite/Maghemite JCPDS 01-082-1533/ 00-039-1346			Hematite JCPDS 01-071-5088			Epsilon JCPDS 00-016-0653		
					XRD Information					
$2\theta°$	d (Å)	d (Å)	hkl	(RI %)	d (Å)	hkl	(RI %)	d (Å)	hkl	(RI %)
35.5	2.48	2.53/2.51	311	(100%)	2.51	110	(72%)	*2.46*	*023*	*(30%)*
62.9	1.45	1.48/1.47	440	(36/34%)	1.45	300	(27%)	*1.47*	*552*	*(30%)*
					SAED Information					
d (Å)		d (Å)	hkl	(RI %)	d (Å)	hkl	(RI %)	d (Å)	hkl	(RI %)
2.94		2.95	220	(35%)		absent		2.98	*−411*	*(35%)*
2.50		2.52	311	(100%)	*2.52*	*110*	*(70%)*	2.46	023	(30%)
2.08		2.09	400	(16%)	*2.08*	*202*	*(3%)*		absent	
1.47		1.47	440	(34%)	*1.49*	*214*	*(30%)*	1.47	552	(30%)

[a] Attributions of low probabilities are in italics; see discussion in the text.

observed, with no trace of γ-Fe_2O_3 or α-Fe_2O_3. This X-ray diffractogram is identical to that of "pure" ε-Fe_2O_3 presented in ref 16. By applying the Scherrer formula, the smallest particles sizes can be estimated at ca. 15 nm. TEM measurements confirm this large size but show that the iron oxide particles are still embedded inside silica. Additional N_2 sorption results reveal that the silica architecture is collapsed. The measured specific surface area of $18 m^2/g$ corresponds to the external surface of silica grains. The diffractogram of the Fe-SBA-B-873,6-27 sample, presented in Figure 2A with a 2θ horizontal scale and in Figure 2B in distances, can also be analyzed without major difficulty. Visual comparison with the stick diagrams summarizing information of JCPDS files indicate the coexistence of α-Fe_2O_3 (main diffraction peak at 2.70 Å, indexed 104, intensity 100%, for instance) and of spinels (ε-Fe_2O_3 or Fe_3O_4, main diffraction peak at 2.48 Å, indexed 311, intensity 100%, for instance). The X-ray diffractograms measured on the Fe-SBA-B-773-27 and Fe-SBA-B-773-67 samples are much more difficult to analyze. Only two small and very broad diffraction peaks (Figure 2A) having a full width at half-maximum larger than 3° in 2θ (Figure 2A) are observed. They indicate ultrasmall oxide particles of poor crystallinity. These peaks are located near $2\theta = 35.5°$ and 62.9° (2.48 and 1.45 Å). Similar peak positions are recorded on a pure maghemite reference sample (dried ferrofluid). As summarized in Table 3, there is an ambiguity of attribution, since these two peaks can also be attributed to reticular planes of α-Fe_2O_3 or ε-Fe_2O_3 varieties. However, these attributions, taking into account planes of low electronic densities, are improbable. Furthermore, the ε-Fe_2O_3 variety can be reasonably eliminated because of the absence of a diffraction peak at 2.72 Å (−420, intensity 100%), clearly detected with the Fe-SBA-B-1373,3-53 sample. Similarly, the α-Fe_2O_3 variety is eliminated because of the absence of a diffraction peak at 2.70 Å (104, intensity 100%) which is clearly observed with the Fe-SBA-B-873,6-27 sample.

A selected area electron diffraction (SAED) image of iron oxide particles formed inside the mesopores of the Fe-SBA-C-873-21 sample (TEM image of the same Fe-loaded silica grain in Figure 3A) is presented in Figure 3C. This image was taken normal to the hexagonal axis of the SBA silica grain. Four distinct series of two spots are observed. Two reticular distances confirm previous X-ray diffraction measurements: 2.50 and 1.47 Å. The two additional ones were not easy to detect in XRD: 2.94 and 2.08 Å. The simultaneous observation of the four distances hamper an attribution to α-Fe_2O_3, since with this variety, no line is expected at 2.94 Å or ε-Fe_2O_3 (no line at 2.08 Å, Table 3). On other images, collected on the Fe-SBA-B-773-67 sample, containing more iron, only the three smallest

distances are observed and the presence of hematite cannot be excluded. The interfringe distances detected on HR-TEM images, shown in Figure 4, yield to distances consistent with attributions to α-Fe_2O_3, γ-Fe_2O_3, or Fe_3O_4. The main interest of these HR-TEM images is to show that the length of coherent domains within FeO_x particles does not exceed 4 to 5 nm.

Micro-Raman spectra have been further used to identify the FeO_x oxides. If the Raman spectra of α-Fe_2O_3, γ-Fe_2O_3, and Fe_3O_4 are well-known[12,34] and present characteristic features, this is not indeed the case for the ε-Fe_2O_3 variety. After the identification of ε-Fe_2O_3 by XRD, a spectrum of this variety has been measured on the Fe-SBA-B-1373,3-57 sample. This spectrum (Supporting Information 2) is extremely complex, and its analysis is far from the objectives of the present paper. The analysis proposed below is only valid for the samples prepared at low temperature (773, 873 K) for which, in view of diffraction results, this variety can be rejected. After this restriction, Raman spectra can be used to distinguish Fe_3O_4, γ-Fe_2O_3, and α-Fe_2O_3. On the micro-Raman spectrum of the Fe-SBA-B-773-27 sample (general view between 200 and 800 cm^{-1}, Figure 5A, and enlargment between 600 and 800 cm^{-1}, Figure 5B), a main broad signal at 722 cm^{-1} is observed, superimposed on the spectrum of silica (one main broad peak ca. 500 cm^{-1}). This broad peak is also observed on a reference ferrofluid (maghemite formed of nanoparticles of 6.6 nm in diameter) sample and can be attributed to oxides of spinel structure, either Fe_3O_4 or γ-Fe_2O_3. On the spectrum of the parent sample containing more iron, Fe-SBA-B-773-53, this broad peak is still detected and associated with narrower peaks located at 396 and 288 cm^{-1}. We attribute these two new peaks to hematite, since peaks are observed at 407 and 290 cm^{-1} on the spectrum of a commercial hematite reference, and the position of the Raman peaks of oxides is known to be sensitive to particles sizes and to shift toward lower frequencies when their size decreases (see, for instance, Raman spectra of ceria in ref 1). Raman spectra can also be used to distinguish Fe_3O_4 and γ-Fe_2O_3. As recently summarized in ref 12, for Fe_3O_4 a main Raman band at 665 cm^{-1} can be attributed to the stretching of oxygen atoms along the Fe−O bonds, whereas in the same spectral range, γ-Fe_2O_3 gives a doublet of peaks, a low-frequency band at ca. 665 cm^{-1}, and a high-frequency one near 720 cm^{-1}. The ratio between the intensities of the first peak and second peak offers a semiquantitative marker for the two phases: Fe_3O_4 gives a ratio of intensity of ca. 1 (mainly short Fe−O distance, vacancy-poor environment), whereas γ-Fe_2O_3 gives a ratio of ca. 0.51 (mainly long Fe−O distance, vacancy-rich environment). On the enlarged spectra (Figure 5B), this peak is located at 722 cm^{-1} for the Fe-SBA-B-773-27 sample and 700 cm^{-1} for the
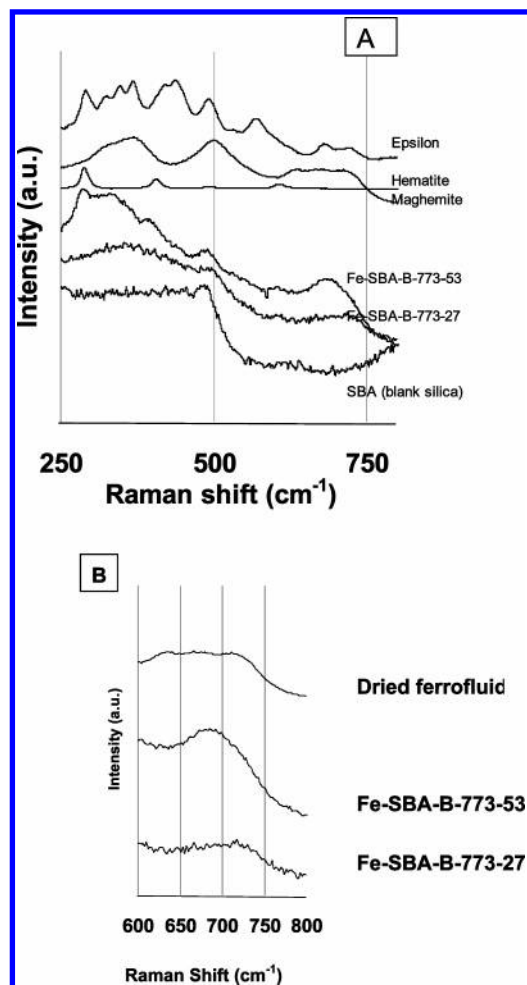
Nanocasting

J. Phys. Chem. B, Vol. 110, No. 51, 2006 **26007**

Figure 5. Raman spectra of selected references (Fe-SBA-B-1373,3-53 for epsilon, commercial hematite, dried ferrofluid for γ varieties; Fe-loaded SBA-B samples. Part A: general view within the range 200–800 cm^{-1}. Part B: enlargment between 600 and 800 cm^{-1}.

Figure 6. Part A: ZFC magnetization loops of sample Fe-SBA-A-773-22 at ($\square$) $T = 300$ K; ($\bigcirc$) $T = 30$ K; ($\bullet$) $T = 5$ K. Right inset, enlargment of the main figure for -10^3 kA/m $\leq H \leq 10^3$ kA/m; left inset: thermal variation of M_S defined as $M(H_{max}, T)/L[\xi(H_{max}, T)]$. Part B: Reduced magnetization $M^* = M/M_S(T)$ as a function of the reduced variable H/T as obtained with sample Fe-SBA-A-773-22 at ($\blacklozenge$) $T = 300$ K and various fields, ($\blacksquare$, ZFC; $\square$, FC) various temperatures and under a field $H = 16$ kA/m, ($\bullet$, ZFC; $\bigcirc$, FC) at various temperatures and under a field $H = 2.4$ kA/m.

Fe-SBA-B-773-53 sample, far away from the 665 cm^{-1} position expected for magnetite. After calcination at 773 K and at low iron concentration (atomic Fe/Si between 0.22 and 0.27), Raman spectra indicate that the short-range atomic order of the oxygen atoms around iron centers is spectroscopically related to maghemite, whereas at higher concentration (atomic Fe/Si ca. 0.53), maghemite and hematite mixtures are detected.

3.3. Magnetic Measurements. Magnetic measurements are performed on Fe-SBA-A-773-22, Fe-SBA-B-773-27, and Fe-SBA-C-773-23 samples. These samples are the more diluted ones, they are prepared with the 1 mol·L^{-1} aqueous solution of iron nitrate, and they mainly contain maghemite.

Let us first analyze in detail the magnetic behavior of one sample: the Fe-SBA-A-773-22. As shown in Figure 6A, the magnetization curve of this sample at room temperature does not exhibit any hysteresis and does not saturate in a field of 4000 kA/m. The high-temperature behavior of this sample is superparamagnetic, and its magnetization M can be adjusted by a simple Langevin formalism $M = m_S \Phi L(\xi)$ where m_S is the magnetization of the nanoparticle material, $\xi = \mu_0 \mu H/kT$ the Langevin parameter, and $L(\xi)$ the Langevin function; μ_0 is the vacuum permability, and $\mu = m_S \pi d^3/6$ the magnetic moment of the nanoparticles (supposedly monodispersed with a diameter d). The room-temperature adjustment leads to $\mu \cong 220\mu_B$ ($\mu_B = 9 \times 10^{-24}$ SI, being the Bohr magneton) and to a saturation magnetization at 300 K $M_S = 1$ emu/g. With the volume fraction Φ being evaluated to 4%, we obtain $m_S \cong 65$ kA/m, and $d \cong$

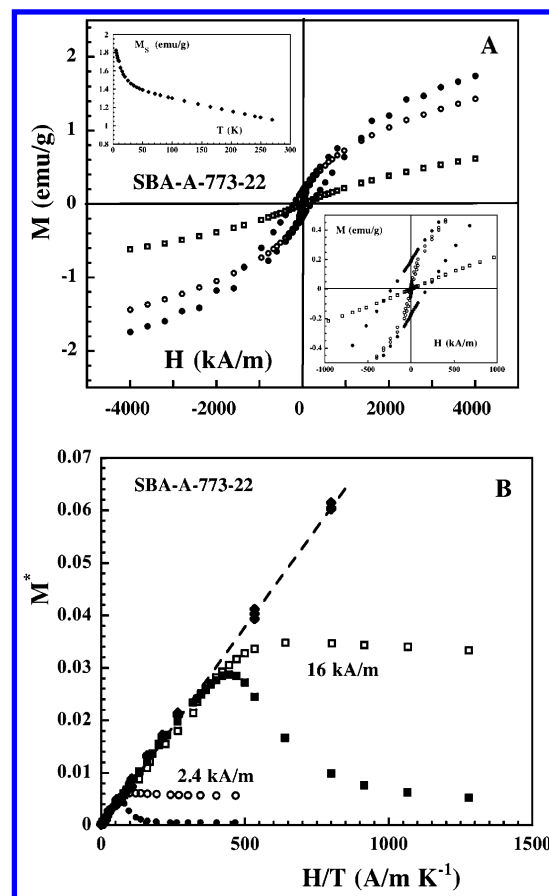4.0 nm (using $\mu = m_S \pi d^3/6$); note that, at $H_{max} = 4000$ kA/m and $T = 300$ K, $L(\xi)$ only reaches a value of 0.61.

With decreasing temperature, hysteretic behavior appears below 35 K. The hysteresis loops recorded at 30 and 5 K are compared in Figure 6A and its right insert: they do not saturate and are open up to large irreversibility fields H_{irr} on the order of 3000 kA/m. At 5 K, the characteristics of the hysteresis loop are a coercivity $H_C \approx 0.05 H_{irr}$ and a remanence $M_R \approx 0.1 M(H = 4000$ kA/m). Let us define M_S as $M(H_{max}, T)/L[\xi(H_{max}, T)]$ where, at the first order, the temperature dependence of μ (through that of m_S) is neglected inside the correction $L[\xi(H_{max}, T)]$. The temperature dependence of M_S is presented in the left insert of Figure 6A. It follows the standard temperature dependence of small iron oxide nanoparticles with a high-temperature behavior close to a Bloch law (with a Bloch constant $B = 4.6 \pm 0.2 \ 10^{-5}$ K$^{-1.5}$) and a low-temperature behavior ruled up by surface effects, as reported in ref 30.

For the same Fe-SBA-A-773-22 sample, the temperature dependence, down to 5 K, of field cooled (FC) and zero field cooled (ZFC) low field magnetization is measured at $H = 2.4$ kA/m and 16 kA/m. Figure 6B plots as a function of H/T the ratios $M^* = M(H, T)/M_S(T)$. This representation[35] attests that, down to ~35 K, temperature below which the irreversibility appears, the ZFC and FC low field magnetizations agree quite well with the Langevin adjusment previously performed at room
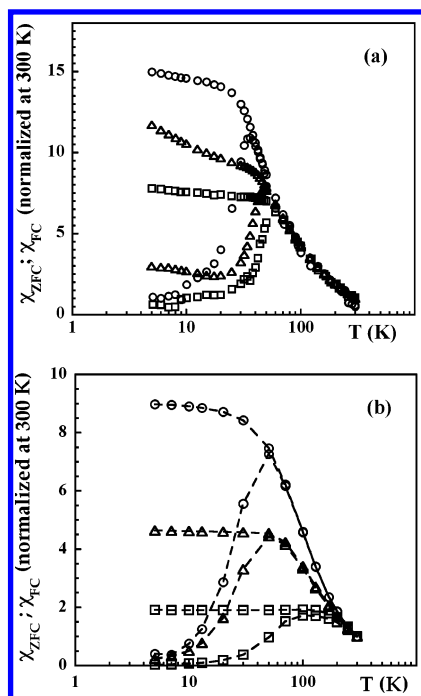
26008 *J. Phys. Chem. B, Vol. 110, No. 51, 2006*

Delahaye et al.

Figure 7. Part A: Field cooled FC and zero field cooled ZFC susceptibilities normalized at 300 K of ○, Fe-SBA-A-773-22; △, Fe-SBA-B-773-27; and □, Fe-SBA-C-773-23. Part B: FF ferrofluids: ○, FFA; △, FFB; and □, FFC.

temperature (still neglecting the temperature dependence of μ). It demonstrates that the magnetic interparticle interactions are negligible here (see Figure 2 of ref 35, for example). This occurs, despite the short interparticle distances seen in TEM, because of the low μ value.

Among all these observations, nothing mimics the striking magnetic behavior of ϵ-Fe$_2$O$_3$ observed in ref 14. Remanence and coercivity are here only observed below 35 K, always lower than the values measured for ϵ-Fe$_2$O$_3$ in that range of temperatures. Moreover, we do not observe any hysteresis at room temperature, and there is no sign of magnetic transition around 80 K. On the contrary, all these measurements show that the magnetic behavior of the nanoparticles of sample Fe-SBA-A-773-22 is close to that of very small sized maghemite nanoparticle.[36-38]

Let us now compare the magnetic properties of Fe-SBA-A-773-22 and Fe-SBA-B-773-27 samples. Room-temperature measurements performed with sample Fe-SBA-B-773-27 lead to very comparable results with $\mu \cong 370\ \mu_B$ and $m_S \cong 65$ kA/m, meaning $d \cong 4.8$ nm. The obtained magnetic diameters determined for Fe-SBA-A-773-22 and Fe-SBA-B-773-27 samples are significantly smaller than the pore diameters of the silica templates determined by N$_2$ sorption (compare Tables 1 and 6).

Finally, let us compare together the three Fe-loaded samples Fe-SBA-A-773-22, Fe-SBA-B-773-27, and Fe-SBA-C-773-23 and compare them to the samples of ferrofluids based on maghemite nanoparticles, FFA, FFB, and FFC, and also to reported data (see ref 36, for example). In Figure 7A are given the field cooled (FC) and zero field cooled (ZFC) magnetizations of the Fe-loaded silicas, as measured at 16 kA/m. They are normalized by their value at 300 K. Tests performed at different fields 2.4 kA/m $\leq H \leq$ 24 kA/m show that the measured magnetization is proportional to the applied field in the whole range of temperatures and, thus, is proportional to an initial susceptibility for these three samples. Similar measurements performed in a linear regime with respect to both H and Φ on

a typical assembly of maghemite nanoparticles at 2.4 kA/m are presented in Figure 7B for the ferrofluid standards FFA, FFB, and FFC. For all the samples (Fe-loaded SBA-15 and ferrofluid FF), the susceptibility at high temperatures is typically superparamagnetic with FC and ZFC measurements coinciding and being proportional to $1/T$. At low temperature, the FC susceptibility continuously increases as the temperature decreases. This confirms the absence of dipolar interactions between the magnetic particles (see ref 35). In parallel, the ZFC susceptibility presents a peak at a temperature T_b which is usually identified with the superparamagnetic blocking temperature of the magnetic moment of the nanoparticles.[36,39] This blocking temperature T_b depends on the sample; its values together with the full width at half-maximum of its peak (fwhm) are given in Table 5 for the standard ferrofluid samples and in Table 6 for the Fe-loaded silica samples. The position and width of the ZFC peak, which are related to the distribution of magnetic anisotropy energy of the nanoparticles (and thus to their magnetic size distribution) provide important insights into the nature of the objects responsible for the observed magnetic behavior. The peaks observed in Figure 7B (width fwhm $\approx 2.3\ T_b$) are much broader than in Figure 7A where fwhm $\approx 1.5\ T_b$ (see Tables 5 and 6). It is thus clear that the polydispersity of the nanoparticles synthesized using the SBA-15 silica solid templates is drastically reduced in comparison to that of the FF samples used here. In addition, the Fe-loaded SBA samples present a peak at a temperature T_b on the same order of magnitude as FFA and FFB samples. Their magnetic sizes are comparable (see Tables 5 and 6), and their energies of anisotropy E_{ani} are also comparable. For FFA and FFB samples, this mean energy is typically on the order of a few 10^{-21} J as previously measured on similar samples by ferromagnetic resonance.[40] Note that the energy of anisotropy derived from the blocking temperature T_b using $E_{ani} \approx 25\ kT_b$[36] would lead to sensibly larger values E_{ani}, on the order of a few 10^{-20} J.

Shifted FC hysteresis loops are observed on both Fe-SBA-A-773-22 and Fe-SBA-C-773-21 samples. These loops remain open up to an irreversibility field on the order of 3×10^3 kA/m with a coercivity on the order of 240 kA/m (see Table 6). For FF samples, much smaller coercivity and irreversibility fields on the order of 100 kA/m are observed (see Table 6 and ref 10), but they are associated to larger magnetic moments. Let us check the coherence of our various magnetic measurements for sample Fe-SBA-A-773-22. Within the hypothesis (usually fulfilled at the nanoscale) that the nanoparticles embedded in the silica matrix are uniaxial, their anisotropy field H_{ani} should be related to their anisotropy energy E_{ani} by the following relation

$$H_{ani} = 2E_{ani}/\mu_0\mu$$

with $\mu = 220\ \mu_B$ and E_{ani} approximately equaling a few 10^{-21} J, it becomes H_{ani} approximately equaling a few 10^3 kA/m, which is on the same order as H_{irr}, the high field limit of irreversibility at low temperature. The measurements are thus indeed self-consistent. They are fully coherent with the observation of very small maghemite nanoparticles.

4. Discussion

4.1. Iron Oxide Variety Patterned inside SBA-15 Silicas. The iron oxide particles patterned inside SBA-15 silicas in Fe-SBA-X-773 samples with Fe/Si atomic ratios ranging between 0.22 and 0.27 are ultrasmall. Using a single characterization technique to identify their nature is difficult. This is mainly due

Nanocasting

J. Phys. Chem. B, Vol. 110, No. 51, 2006 **26009**

TABLE 4: Association of Preparation Conditions, XRD, SAED, and Raman Data to Solve Ambiguities of Attributions in FeO_x Nanoparticles Mn, Magnetite; Mh, Maghemite; H, Hematite; and E, Epsilon (see details in the text)

samples	preparation conditions	XRD	SAED	Raman	attribution
Fe−SBA-A-773−22	temperature too low for epsilon	(Mh/Mn)	(Mh/Mn)	Mh	Mh
Fe−SBA-B-773−27	(Mh/Mn), H				
Fe−SBA-C-773−23					
Fe−SBA-B-773−67	temperature too low for epsilon	(Mh/Mn), H	(Mh/Mn), H	Mh, H	Mh, H
Fe−SBA-C-873−27	(Mh/Mn), H				
Fe−SBA-B-873,6−46	Temperature too low for epsilon (Mh/Mn), H	Mh, H		Mh, H	Mh, H
Fe−SBA-B-1373,3−53	E, traces of hematite possible	E		E	E

TABLE 5: Magnetic Characteristics of the Ferrofluid Samples (FF)[a]

sample	Φ (%)	m/m_B	m_S	d_0 (nm)	s	T_b (K)	fwhm (K)	H_C^{ZFC} (kA/m)
FFA	0.44	560	190	3.7	0.33	40	90	5.2
FFB	0.12	4.5×10^3	270	6.6	0.22	50	137	17
FFC	0.04	1.55×10^4	295	9.7	0.29	100	∼270	16

[a] Φ: volume fraction of nanoparticles as measured by chemical titration of iron. μ: magnetic moment of the nanoparticles as deduced from a Langevin fit of the room-temperature magnetization, expressed in unit of Bohr magnetons μ_B. m_S: saturation magnetization of the nanoparticles as obtained from the Langevin fit of the room magnetization. d: diameter of the nanoparticules as deduced from μ and m_S, using $\mu = m_S \pi d^3/6$. T_b: blocking temperature as obtained from the maximum of ZFC susceptibility (see Figure 7). fwhm: full width at half-maximum of ZFC susceptibility from Figure 7. H_C^{ZFC}: coercivity at 5 K of ZFC magnetization loops.

TABLE 6: Magnetic Characteristics of Fe-Loaded SBA-15 Silicas[a]

sample	D_{PORE} (nm)	μ/μ_B	m_S kA/m	d (nm)	T_b (K)	fwhm (K)	H_C^{FC+} (kA/m)	H_C^{FC-} (kA/m)
Fe−SBA-A-773−22	4.3	220	65	4.0	36	52	+210	−320
Fe−SBA-B-773−27	6.6				48	74		
Fe−SBA-C-773−23	9.5	370	65	4.8	58	86	+230	−315

[a] D_{PORE}: pore diameter of the silica template as obtained by N_2 sorption (see Table 1). μ: magnetic moment of the nanoparticles as deduced from a Langevin fit of the room-temperature magnetization, expressed in unit of Bohr magnetons μ_B. m_S: saturation magnetization of the nanoparticles as obtained from the Langevin fit of the room magnetization. d: diameter of the nanoparticules as deduced from μ and m_S, using $\mu = m_S \pi d^3/6$. T_b: blocking temperature as obtained from the maximum of ZFC susceptibility (see Figure 7). fwhm: full width at half-maximum of ZFC susceptibility from Figure 7. H_C^{FC+} and H_C^{FC-}: coercivities at 5 K of FC magnetization loops, field cooled under 16 kA/m.

to a lack of crystallinity, which is related to the dispersion of FeO_x particles inside the pores of SBA-15 silicas. As evidenced in Figure 2, larger and much more crystalline particles are observed for the Fe-SBA-B-873,6-27 and Fe-SBA-B-1373,3-53 samples in which the silica framework is collapsed.

As summarized in Table 4, in the absence of clear identification by XRD, ambiguities of attribution can be solved by combining chemical aspects (conditions of preparation), structural X-ray diffraction, SAED measurements, and spectroscopic micro-Raman information. Micro-Raman spectroscopy is, in theory, particularly helpful to distinguish iron oxide polymorphs. The analysis of spectra is, indeed, less reliant on crystallinity than XRD for phase identification. However, since several peak positions are common to the ϵ-Fe_2O_3 variety and other polymorphs, this technique is helpful only if diffraction data showing that the ϵ-Fe_2O_3 variety can be rejected are available. On the basis of this combined approach, maghemite seems to be the main component only in the Fe-SBA-X-773-21 to 27 or Fe-SBA-X-873-21 to 27 samples, corresponding to an Fe/Si atomic ratio within the range 0.21−0.27, thermally treated at 773 or 873 K and quenched to room temperature. For the sample Fe-SBA-B-873,6-27 maintained at 873 K, 6 h, a mixture of hematite and maghemite is detected. A similar mixture is formed in the Fe-SBA-B-773-67, having an Fe/Si atomic ratio of 0.67. This suggests that the selective formation of maghemite critically depends on three experimental factors: (i) the calcination temperature, (ii) kinetic aspects (time of calcination at 873 K), and (iii) the iron amount.

4.2. Thermal Stability of the Maghemite Ultrasmall Particles Patterned in SBA-15. The nanoparticles of Fe_2O_3 obtained by nanocasting in ordered silicas described so far were all corresponding to the hematite variety. The samples with Fe/Si atomic ratios ranging between 0.22 and 0.27 described here

mainly contain maghemite and most probably differ for three main reasons: (1) differences in experimental conditions (iron salt precursor, technique used to deposit this salt within the pores, thermal treatment used to transform it to oxides), (2) differences in iron content and hence iron oxide nanocrystals dimensions, or (3) differences in the location of the iron oxide particles inside the pores or on the external surface of silica grains. In some former publications, iron oxide particles larger than mesopore dimensions, and then most probably located outside silica grains, have indeed been clearly identified.[21,22] However, the iron oxide variety is not determined only by the nanoparticle location, since the Fe-SBA-B-773-67 sample contains a mixture of maghemite and hematite, and TEM fails to detect a large amount of iron oxide particles outside the silica grains. This last observation, associated with the kinetic aspects introduced above, rather suggests that the formation of hematite is associated with a minimal size of the FeO_x particles which, for a given calcination temperature, is controlled by their dispersion within the pores and by the iron content. Increasing the size of γ-Fe_2O_3 nanoparticles helps their transformation into α-Fe_2O_3. At low iron content, ultrasmall particles of γ-Fe_2O_3 nanoparticles are formed within the pores and their aggregation is hampered by their dispersion, which further avoids the formation of α-Fe_2O_3. With larger iron amounts, the volume fraction between growing iron oxide particles decreases. Diffusion giving large oxide particles, with some of them being large enough to be transformed into α-Fe_2O_3, can be formed inside the pores of the silica templates.

4.3. Magnetic Measurements as a Tool to Compare the Surface Properties of Maghemite Particles in Fe-SBA-X-773-21 to 27 Samples Patterned in SBA-15 Silicas or Citrate-Coated. Besides the ultrasmall size evaluation of the maghemite particles present in these samples, several experimental observa-

tions support the existence of peculiar surface effects. Loops open up to very large fields, shifted FC loops, nonsaturation in a large field, large coercitivity, and low-temperature cusp in the nanoparticle magnetization are all typical observations usually associated with surface effects which are reported in very small ferrite nanoparticules (typically below 5 nm; see, for example, refs 2, 3, 30, 37, 39, and 41). All these observations are present both experimentally and in Monte Carlo calculations on small core−shell magnetic nanoparticles.[42] Moreover, both experimentally and in Monte Carlo calculations, a second maximum in the ZFC magnetization at very low temperature (typically below 10 K) has been observed and attributed to the blocking temperature of surface spins.[40] A small cusp below 10 K can be guessed for nanoparticles synthesized in the SBA matrix and could be attributed to the freezing of such surface spins in the same way. In small maghemite nanoparticles, it is indeed reasonable to think of a magnetic core/shell structure, with the monodomain magnetic core being surrounded by a shell of disordered and badly coupled individual spins. These surface spins fluctuating at high temperatures and freezing at low temperatures[39,43] give an important contribution to the magnetic energy of anisotropy which is standardly observed with FF samples such as FFA.[6,40] However, in standard FF samples based on spherical nanoparticles, as these probed here, such a strong coercitivity have never been observed until now. In the case of γ-Fe$_2$O$_3$ nanoplatelets, a coercivity associated to surface freezing,[39] and being half that observed here, has been reported in the same range of temperatures as for our samples, meaning that the influence of the surface spins is even larger here. Moreover, a similarly large coercitivity has already been reported for γ-Fe$_2$O$_3$ nanoparticles embedded inside amorphous silica obtained by sol−gel techniques. As proposed by Caizer et al.,[13] specific surface Fe−O−Si can be responsible for the modification of superexchange interactions. It is important to notice that, in this former study, the silica porous matrix was generated by spontaneous condensation of alkoxysilane (nanopores with a broader size distribution than the well-calibrated mesopores of the SBA-15 silicas used here), and larger iron oxide particles were described (10.2 and 9.4 nm in diameter).

5. Conclusions and Outlook

We have prepared ultrasmall FeO$_x$ nanoparticles by nanocasting inside the pores of SBA-15 silica templates. The pores of the silica template act as a dispersing medium, increasing the average spacing between the nanoparticle nucleation sites and also as a mold to limit their growth upon calcination. The growth of FeO$_x$ particles outside the silica grains has been avoided by depositing the iron precursor (iron(III) nitrate) inside the pores by using the two-solvents technique (under mild conditions). By calcination in air at 773 or 873 K (followed by quenching to room temperature) and at low iron loading (atomic Fe/Si ratio 0.22 to 0.27), nanoparticles of poor crystallinity are formed. In these particles, the oxygen atoms surrounding Fe-(III) centers are spectroscopically related to maghemite. Mixtures of hematite and maghemite are observed with less diluted samples (atomic Fe/Si ratio of 0.67) and also under more drastic calcination conditions (873 K maintained 6 h). Upon heating to 1373 K, pure ϵ-Fe$_2$O$_3$ particles, with a crystallinity identical to particles formed by sol−gel,[16] are generated. Unfortunately, under the heat treatment conditions described here, the porosity of the SBA-15 silica collapses, and ϵ-Fe$_2$O$_3$ particles with diameters larger than 15 nm are formed. It is clear that optimized conditions giving smaller particles of this variety remain to be defined.

By calcination in air at 773 K, ultrasmall γ-Fe$_2$O$_3$ nanoparticles of low magnetization are obtained. They are superparamagnetic at room temperature, have a narrow dispersion, and do not magnetically interact together in the explored range of temperatures. Their strong surface effects, directly correlated to their small size, could be related to modifications of superexchange interactions at their surface via specific particle−silica walls interactions.

Like the solids recently described in ref 44, the Fe-loaded SBA samples that we have prepared are interesting as supports for catalytic application for two reasons: (i) the main silica component can easily be functionalized and (ii) the presence of γ-Fe$_2$O$_3$ nanoparticles impart magnetic properties making the solids easily extracted from reacting media (solvents for instance) after use. Another interest of our study is to show that, because of their dispersion, nanoparticles of a metastable oxide such as γ-Fe$_2$O$_3$ can be obtained by nanocasting in SBA-15 silicas. The dispersion-induced thermal stabilization observed here is probably not limited to iron oxides. Its application to other couples of oxides (titania and anatase/rutile, for instance) whose temperature of transformation is correlated with aggregation processes and particles sizes is certainly a valuable way to enlarge the field of application of SBA-15 silicas.

Supporting Information Available: Additional experimental data. This material is available free of charge via the Internet at http://pubs.acs.org.

References and Notes

(1) Fernandez-Garcia, M.; Martinez-Arias, A.; Hanson, J. C.; Rodriguez, A. *Chem. Rev.* **2004**, *104*, 4063 and references therein.

(2) Battle, X.; Labarta, A. *J. Phys. D* **2002**, *35*, R15.

(3) *Surface Effects in Magnetic Nanoparticles*; Fiorani, D., Ed.; Springer: New York, 2005.

(4) Néel, L. *J. Phys. Radium* **1954**, *15*, 225.

(5) Aharoni, A. *J. Appl. Phys.* **1988**, *63*, 4605.

(6) Raikher, Y. L.; Perzynski, R. In *Surface Effects in Magnetic Nanoparticles*; Fiorani, D., Ed.; Springer: New York, 2005; p 14.

(7) Tronc, E.; Nogues, M.; Chaneac, C.; Lucari, F.; D'Orazio, F.; Greneche, J. M.; Jolivet, J. P.; Fiorani, D.; Testa, A. M. *J. Magn. Magn. Mater.* **2004**, *272−276*, 1474.

(8) Iglesias, O.; Labarta, A. *J. Magn. Magn. Mater.* **2004**, *272−276*, 685.

(9) Veintemillas-Verdaguer, S.; Morales, M. P.; Serna, C. J. *Mater. Lett.* **1998**, *35*, 227.

(10) Martinez, B.; Roig, A.; Obradors, X.; Molins, E.; Rouanet, A.; Monty, C. *J. Appl. Phys.* **1996**, *79*, 2580.

(11) Massart, R. *IEEE Trans. Magn. Magn.* **1981**, *17*, 1247.

(12) Long, J. W.; Logan, M. S.; Rhodes, C. P.; Carpenter, E. E.; Stroud, R. M.; Rolison, D. R. *J. Am. Chem. Soc.* **2004**, *126*, 16879.

(13) Caizer, C.; Hrianca, I. *Eur. Phys. J. B* **2003**, *31*, 391. Caizer, C.; Savii, C.; Popovici, M. *Mater. Sci. Eng.* **2003**, *B97*, 129.

(14) Gich, M.; Roig, A.; Frontera, C.; Molins, E.; Sort, J.; Popovici, M.; Chouteau, G.; Martin y Marero, D.; Nogues, J. *J. Appl. Phys.* **2005**, *98*, 044307. Gish, M.; Frontera, C.; Roig, A.; Fontcuberta, J.; Molins, E.; Bellido, N.; Simon, Ch.; Fleta, C. *Nanotechnology* **2006**, *17*, 687.

(15) Popovici, M.; Gich, M.; Niznansky, D.; Roig, A.; Savii, C.; Casas, L.; Molins, E.; Zaveta, K.; Enache, C.; Sort, J.; De Brion, S.; Chouteau, G.; Nogues, J. *Chem. Mater.* **2004**, *16*, 5542.

(16) Tronc, E.; Chaneac, C.; Jolivet, J. P.; Greneche, J. M. *J. Appl. Phys.* **2005**, *98*, 053901. Tronc, E.; Chaneac, C.; Jolivet, J. P. *J. Solid State Chem.* **1998**, *139*, 93.

(17) Jansen, A. H.; Yang, C. M.; Wang, Y.; Schüth, F.; Koster, A. J.; de Jong, K. P.; *J. Phys. Chem. B* **2003**, *107*, 10552.

(18) Crowley, T. A.; Ziegler, K. Z.; Lyons, D. M.; Erts, D.; Olin, H.; Morris, M. A.; Holmes, J. D. *Chem. Mater.* **2003**, *15*, 3518.

(19) Abe, T.; Tachinaba, Y.; Uematsu, T.; Iwamoto, M. *Chem. Commun.* **1995**, 1617.

(20) Yuan, Z. Y.; Liu, S. Q.; Chen, T. H.; Chang, J. Z. *Chem. Commun.* **1995**, 973.

(21) Köhn, R.; Paneva, D.; Dimitrov, M.; Tsoncheva, T.; Mitov, I.; Minchev, C.; Fröba, M. *Microporous Mesoporous Mater.* **2003**, *63*, 125.

(22) Bengoa, J. F.; Cagnoli, M. V.; Gallegos, N. G.; Alvarez, A. M.; Mogni, L. V.; Moreno, M. S.; Marchetti, S. G. *Microporous Mesoporous Mater.* **2005**, *84*, 153.

(23) Fröba, M.; Köhn, R.; Bouffard, G.; Richard, O.; Van Tendeloo, G. *Chem. Mater.* **1999**, *11*, 2858.

(24) Ryoo, R.; Joo, S. H.; Jun, S. *J. Phys. Chem. B* **1999**, *1003*, 7743.

(25) Impéror-Clerc, M.; Bazin, D.; Baunier, P.; Appay, M. D.; Davidson, A. *Chem. Mater.* **2004**, *16*, 1813. Escax, V.; Impéror-Clerc, M.; Bazin, D.; Davidson, A. *C. R. Acad. Sci.* **2005**, *3−4*, 663.

(26) Zhao, D.; Feng, J.; Huo, Q.; Melosh, N.; Stucky, G. D. *Science* **1998**, *279*, 548.

(27) Massart, R.; Dubois, E.; Cabuil, V.; Hasmonay, E. *J. Magn. Magn. Mater.* **1995**, *149*, 149.

(28) Matos, J. R.; Mercuri, L.; Kruk, M.; Jaroniek, M. *Chem. Mater.* **2001**, *13*, 1726.

(29) De Faria, D. L. A.; Silva, S. V.; de Oliviera, M. T. J. *J. Raman Spectrosc.* **1997**, *28*, 873.

(30) Aquino, R.; Depeyrot, J.; Sousa, M.; Tourinho, F. A.; Dubois, E.; Perzynski, R. *Phys. Rev. B* **2005**, *72*, 184435 and references therein.

(31) Ravikovitch, P. I.; Neimark, A. V. *Langmuir* **2002**, *18*, 9830.

(32) Jansen, A. H.; Yang, C. M.; Wang, Y.; Schüth, F.; Koster, A. J.; de Jong, K. P. *J. Phys. Chem. B* **2003**, *107*, 10552.

(33) Nasrazadani, S.; Raman, A. *Corros. Sci.* **1993**, *34*, 1355.

(34) Oh, S. J.; Cook, D. C.; Townsend, H. E. *Hyperfine Interact.* **1998**, *112*, 59.

(35) Mamiya, H.; Nakatani, I.; Fubayashi, T. *Phys. Rev. Lett.* **1998**, *80*, 177.

(36) Park, J.; An, K.; Hwang, Y.; Park, J.-G.; Noh, H.-J.; Kim, J.-Y.; Park, J.-H.; Hwang, N.-M.; Hyeon, T. *Nat. Mater.* **2004**, *3*, 891.

(37) Kachkachi, H.; Ezzir, A.; Nogues, M.; Tronc, E. *Eur. Phys. J. B* **2000**, *14*, 681.

(38) Aquino, R.; Gomes, J. A.; Tourinho, F. A.; Dubois, E.; Perzynski, R.; da Silva, G. J.; Depeyrot, J. *J. Magn. Magn. Mater.* **2005**, *289*, 431.

(39) Martinez, B.; Obradors, X.; Balcells, L.; Rouanet, A.; Monty, C. *Phys. Rev. Lett.* **1998**, *80*, 181.

(40) Gazeau, F.; Bacri, J. C.; Gendron, F.; Perzynski, R.; Raikher, Yu. L.; Stepanov, V.; Dubois, E. *J. Magn. Magn. Mater.* **1998**, *186*, 175.

(41) Kodama, R. H.; Berkowitz, A. E.; McNiff, E. J.; Foner, S. *Phys. Rev. Lett.* **1996**, *77*, 394.

(42) Zysler, R. D.; de Biasi, E.; Ramos, C. A.; Fiorani, D.; Romero, H. In *Surface Effects in Magnetic Nanoparticles*; Fiorani, D., Ed.; Springer: New York, 2005; p 239.

(43) Gazeau, F.; Dubois, E.; Hennion, M.; Perzynski, R.; Raikher, Yu. L. *Europhys. Lett.* **1997**, *40*, 575.

(44) Yi, D. K.; Lee, S. S.; Ying, J. Y. *Chem. Mater.* **2006**, *18*, 2459.